

Quantitative analysis of directional spontaneous emission spectra from light sources in photonic crystals

Ivan S. Nikolaev,^{*} Peter Lodahl, and Willem L. Vos

*Complex Photonic Systems (COPS),
Department of Science and Technology,
and MESA⁺ Institute of Nanotechnology,
University of Twente, PO Box 217,
7500 AE Enschede, The Netherlands.[†]*

(Dated: Original manuscript submitted on July 26th, 2004)

Abstract

We have performed angle-resolved measurements of spontaneous-emission spectra from laser dyes and quantum dots in opal and inverse opal photonic crystals. Pronounced directional dependencies of the emission spectra are observed: angular ranges of strongly reduced emission adjoin with angular ranges of enhanced emission. It appears that emission from embedded light sources is affected both by the periodicity and by the structural imperfections of the crystals: the photons are Bragg diffracted by lattice planes and scattered by unavoidable structural disorder. Using a model comprising diffuse light transport and photonic band structure, we quantitatively explain the directional emission spectra. This provides detailed understanding of the transport of spontaneously emitted light in real photonic crystals, which is essential in the interpretation of quantum-optics in photonic band-gap crystals and for applications wherein directional emission and total emission power are controlled.

PACS numbers: 42.50.Nn, 42.70.Qs, 78.67.Hc, 42.50.Ct, 42.25.Fx, 81.05.Zx

^{*}Electronic address: i.nikolaev@utwente.nl

[†]URL: www.photonicbandgaps.com

I. INTRODUCTION

Photonic crystals attract much attention both in academia and in industry because they offer exciting ways of manipulating photons [1]. Periodic variations of the refractive index in photonic crystals on a length scale of the wavelength of light cause optical Bragg diffraction and organize the photon dispersion relation in bands, analogous to electron bands in semiconductors [2, 3, 4]. Frequency windows, called stop gaps, appear in which there are no modes for certain propagation directions. Photonic structures already serve as a base for controlling the propagation of light. Of even greater interest are three-dimensional (3D) photonic crystals that summon novel opportunities in the case of a photonic band gap (PBG) - a frequency range where no modes exist at all. The existence of a gap in the density of photonic modes leads to novel quantum-optical phenomena such as spontaneous emission inhibition, light localization [2, 3, 4, 5, 6].

Control over the radiative decay rate of spontaneous emission is of keen interest for applications, and therefore emission properties of sources such as atoms, dyes, and quantum dots are intensively investigated. According to Fermi's 'Golden Rule', this decay rate is proportional to the local radiative density of states (LDOS) that counts the number of electromagnetic modes wherein photons can be emitted at a specific location of the source. In 3D photonic crystals pronounced variations of the LDOS with frequency are predicted even in the absence of a PBG [7, 8], which give rise to angle-independent variations of the total emission. Recently LDOS effects on spontaneous emission have been experimentally demonstrated: Using inverse opals photonic crystals considerable variations of the emission rates in large band widths were obtained in both continuous-wave (cw) total-emission power experiments [9] and in time-resolved lifetime experiments [10]. While lifetime experiments provide a direct measurement of decay rates, it is important to quantitatively interpret concomitant emission spectra, for instance, to confirm that light sources inside the crystal are probed. Cw experiments, on the other hand, rely on a comparison of angle-integrated spectra with a homogeneous medium. In the latter case a complete understanding of all angle-dependent effects, that is, Bragg diffraction on the propagation of light is crucial. In this paper such a quantitative analysis is presented.

In contrast to decay rates, emission spectra of sources embedded in photonic crystals are strongly directional [11, 12, 13, 14, 15, 16]. Particular frequency ranges of the spectra

are suppressed in certain directions forming stop gaps, whose center frequencies and the widths are described by the photon dispersion relation. Besides Bragg diffraction, which is an effect of the order of the periodic structure, light propagating inside the structure also *feels* disorder: polydispersity, roughness and misarrangements of the building blocks [17]. This unavoidable disorder affects the interference-induced properties of photonic crystals. Previous work on the effect of disorder on spontaneous emission includes the realization that disorder determines the depth of stop gaps [13, 15] and the observation of disorder-induced enhanced emission in the range of first and second-order stop gaps [18]. While the propagation of light from external light sources has been studied in great detail [19, 20], a quantitative explanation of the behavior of light emission from internal sources has lacked so far.

Here we present strongly frequency-dependent angular distributions of spontaneous emission from a laser dye in polystyrene opals and from quantum dots in titania inverse opals in the frequency range around the first-order Bragg diffraction (L-gap). We compare the data to a theoretical model that unifies effects of structural disorder and photonic crystal properties [21]. Angle-dependent internal reflection due to the photonic gaps plays a key role in our model. The theory quantitatively explains both the enhancement and the reduction of light along certain propagation directions that were observed experimentally. The excellent agreement confirms that the propagation of light in a photonic crystal is well understood for frequencies around the L-gap. Furthermore, we show that by analyzing the exit emission distributions, one can reveal stop gaps in the quantum dot spectra. Such an analysis should be carefully performed before any quantum-optical experiments since it unambiguously proves the effect of the photonic crystal on emission. We finally discuss the applicability of photonic crystals for improvement of the emission efficiency of light sources.

II. EXPERIMENTAL DETAILS

A. Samples

We have studied emission from dyes in polystyrene opals and from quantum dots in titania inverse opals. The polystyrene opals are fcc crystals of close-packed polystyrene spheres prepared from a colloidal suspension by self-assembly. The titania inverse opals are

fcc structures of close-packed air spheres in a solid matrix of TiO_2 . Details of the preparation and characterization of the opals and inverse opals can be found in Ref. [22]. We have studied 4 polystyrene samples with lattice parameters $a = 178 \pm 3$ and 365 ± 5 nm and 8 titania samples with lattice parameters $a = 370, 420, 500, 580$, and 650 ± 10 nm. All samples have typical dimensions of $2 \times 2 \times 0.2$ mm³ and contain high-quality domains with diameters larger than $50 \mu\text{m}$. These domains have flat faces normal to the 111 crystal axis, which is evident from SEM images. The other crystalline axes are randomly oriented.

The polystyrene opals were doped with the laser dye Rhodamine 6G (R6G) by immersing them into a dilute solution (10^{-6} mol/l) of the dye in ethanol. We estimate to have about 10 dye molecules per sphere. This number is sufficiently low to avoid reabsorption or energy transfer processes [23]. Afterwards the samples were rinsed in ethanol and dried. In order to ensure that the emission was recorded only from the bulk of the crystal, and not from the crystal surface, the dye absorbed near the surface was bleached [13]. The whole surface was illuminated by an intense laser beam at the Bragg angle for the pump frequency. At this angle the pump intensity decreases exponentially with depth, which implies that the dye bleaches within the first few crystal layers.

The titania inverse opals were infiltrated for 24 hours with a colloidal suspension of ZnSe-coated CdSe quantum dots [24, 25] in a mixture of 50% chloroform and 50% butanol. Afterwards the samples were rinsed in chloroform and dried. The concentration of the infiltrating solution was 10^{-7} mol/l. In order to minimize oxidation and contamination of the quantum dots, the inverse opals doped with quantum dots were prepared in a nitrogen-purged glove box and held in a sealed chamber under a 1.7 mbar nitrogen atmosphere during the optical measurements.

B. Experimental set-up

Figure 1 shows the experimental set-up used to measure emission from light sources inside photonic crystals. The sources inside the crystal are excited by a *cw* Ar-ion laser ($\lambda = 497$ nm) with the power at the sample below $10 \mu\text{W}$. To focus the pump beam on the sample surface a fiber-coupled microscope objective is used. The beam is focused to a spot of about $30 \mu\text{m}$ in diameter at an incident angle θ_p , usually $\theta_p \approx 25^\circ$. In order to acquire emission spectra as a function of the detection angle θ_e relative to the surface

normal, the sample is mounted on a rotation stage. The surface normal is parallel to the 111 reciprocal lattice vector G_{111} . In order to illuminate the same area irrespective of θ_e , the fiber-coupled objective (O_1) is mounted on the same rotation stage as the sample. In this way, the angle of incidence θ_p between the pump beam and the surface normal is kept constant. The advantage over previous experiments, where the sample was rotated with respect to both the pump and detection beams, is that the absolute intensity of the angle-dependent spectra can be reliably compared. The position of the pump spot on the sample is monitored with a microscope. The emitted light is collected within a cone of 15° full width around the angle θ_e , imaged on the slit of the spectrometer with 4 nm resolution, and detected by the photomultiplier tube (PMT). The angle-resolved spectra are usually measured at the detection angles from 0° to 75° at intervals of 15° . The measured spectra are corrected for the dark count of the PMT. The shapes of the spectra are confirmed to be independent of the pump intensity, and the emitted intensity is linear with the pump power.

III. DIFFUSE LIGHT TRANSPORT IN PHOTONIC CRYSTALS

A. Escape function

In real photonic structures, defects in the arrangement of the building blocks are always present and cause random multiple scattering of light. This means that all light emitted in such photonic structures becomes diffuse on length scales equal to the transport mean free path l , which is often much smaller than the thickness of the sample L . For example, our opals and inverse opals have mean free paths of about $15\ \mu\text{m}$, whereas the thickness of the samples is about $200\ \mu\text{m}$ [26]. Thus, even though emission inside a photonic crystal is diffracted by the crystal structure, this effect is smeared out by the random multiple scattering while the light propagates through the bulk. Only at distances from the surface z smaller than l , where photons emanate ballistically towards the crystal-air interface after a last scattering event, the effect of Bragg diffraction is not destroyed by the scattering. Hence the diffuse emission acquires a directional dependence only when it exits the crystal [21].

We consider the ratio of the mean free path l to the attenuation length for Bragg diffraction L_B in order to estimate the attenuation of emission caused by Bragg diffraction as proposed in Ref. [15]. Since the mean free path l is larger than the Bragg attenuation

length L_B (typically $l/L_B \sim 2 - 5$ [26]), an attenuation in the stop band equal to $1 - L_B/l = 50\%$ to 80% is predicted, in agreement with our observations.

In the present work we investigate directional properties of light emitted by sources from 3D photonic crystals and compare to a model of diffuse light transmission through opaque media [27, 28, 29] extended to photonic crystals [21]. Based on the diffusion theory, the intensity of light $I(\omega, \mu_e)$ with frequency ω that exits the sample at external angles between $\theta_e = \cos^{-1}(\mu_e)$ and $\cos^{-1}(\mu_e + d\mu_e)$ relative to the surface normal is equal to

$$I(\omega, \mu_e)d\mu_e = I_{tot}(\omega)P(\omega, \mu_e)d\mu_e. \quad (1)$$

Here $I_{tot}(\omega)$ is the total spontaneous emission power that is the spectrum of the light sources integrated over the exit angles θ_e . For sources with a low quantum efficiency or with inhomogeneously broadened spectra, $I_{tot}(\omega)$ is proportional to the LDOS [9]. The distribution $P(\omega, \mu_e)$ is defined as

$$P(\omega, \mu_e) = \mu_e \frac{n_e^2}{n_i^2} \left(\frac{1 + \bar{R}(\omega)}{1 - \bar{R}(\omega)} + \frac{3}{2}\mu_i \right) [1 - R(\omega, \mu_i)], \quad (2)$$

where n_e and n_i are average refractive indices outside and inside the sample [30], respectively. μ_e and μ_i are related by Snel's law. $R(\omega, \mu_i)$ are angle-dependent internal-reflection coefficients, that yield an angle-averaged internal-reflection coefficient $\bar{R}(\omega)$:

$$\bar{R}(\omega) = \frac{3C_2(\omega) + 2C_1(\omega)}{3C_2(\omega) - 2C_1(\omega) + 2}, \quad (3)$$

$$C_n(\omega) = \int_0^1 R(\omega, \mu_i) \mu_i^n d\mu_i. \quad (4)$$

From diffusion theory, $\bar{R}(\omega)$ determines the so-called extrapolation length that sets the boundary conditions of the diffuse intensity [27, 28, 29]. The normalized function $P(\omega, \mu_e)$ describes the distribution of emission intensity over the escape angles and will be called the ‘escape function’. In absence of reflection effects, the escape distribution tends to the well-known Lambertian distribution of diffuse surfaces.

The angular dependence of the escape function $P(\omega, \mu_e)$ agrees well with experiments on random media, if an average refractive index and Fresnel's reflection coefficients are used to model $R(\omega, \mu_i)$ [28, 29]. In random media such as powders or macroporous sponges the internal-reflection coefficient $R(\omega, \mu_i)$ is barely frequency dependent [31]. However, for highly dispersive photonic crystals Fresnel's model cannot describe the internal reflection.

Light escaping from a depth $z < l$ from the crystal surface is Bragg attenuated for angles and frequencies matching the Bragg condition. Hence a strongly angle and frequency-dependent internal reflection due to the photonic band structure plays a key role in the escape distribution of diffuse emission.

B. Internal-reflection coefficient

In order to model the internal-reflection coefficient $R(\omega, \mu_i)$, we have taken into consideration calculated photonic band structures. Figure 2(a) shows the photonic band structure for polystyrene opals calculated along the LU and LK lines in reciprocal space in the frequency range around the first-order stop gap (L-gap) that is due to optical Bragg diffraction by (111) planes parallel to the sample surface. The emission spectrum of R6G is in the low-frequency limit relative to the stop bands of opals with a lattice parameter $a = 178$ nm (region confined by the orange dash-dot-dotted lines). Consequently, this sample is effectively homogeneous for the emission frequencies, and therefore it can serve as a reliable reference. For these nonphotonic crystals we used Fresnel's model in order to describe the internal reflection. In Figure 2(a) one can also see the frequency gap between the two lowest bands (blue dashed curves), which obeys Bragg's law (red curve) within the frequency range of R6G emission for the opals with a lattice parameter $a = 365$ nm (region confined by the green dash-dotted lines). Therefore, the angular dependence of the center frequency of the L-gap is modelled with the red curve, i.e.: $\omega_C(\mu_i) = \omega_C(\mu_i = 1)/\mu_i$. To investigate the frequency dependence of the reflectivity, we have performed reflectivity experiments on the samples using external incident plane waves, since this technique reveals the center frequencies and the widths of stop gaps [20, 32]. Figure 2(b) shows a normal-incidence reflectivity spectrum measured from an opal with the lattice parameter $a = 365$ nm (blue circles). The reflectivity peak is not fitted well with a Gaussian (red dashed curve). As an improved model, we propose a modified Gaussian (Fig. 2(b), black curve):

$$R_1(\omega, \mu_i) = A_1(\mu_i) \exp \left[- \frac{(\omega - \omega_C(\mu_i))^4}{2(\Delta\omega_C(\mu_i))^4} \right], \quad (5)$$

where $A_1(\mu_i)$ is the magnitude of the internal-reflection coefficient and $\Delta\omega_C(\mu_i)$ is the width parameter. This peak shape is seen to fit the measurements well for frequencies > 16000 cm^{-1} . At low frequencies below 16000 cm^{-1} a deviation from the model is observed. We

attribute this deviation to Fresnel's reflection, which is important only in the low-frequency limit and therefore is not relevant for the escape function of photonic samples. The width of the L-gap $\Delta\omega_C(\mu_i)$ hardly varies with μ_i within the range of the dye emission, therefore it is taken to be constant in our model. The magnitude of the internal-reflection coefficient $A_1(\mu_i)$ decreases with μ_i because at larger internal angles $\theta_i = \cos^{-1}(\mu_i)$ the path length for the light to become Bragg attenuated increases with μ_i , and this increases the probability of scattering at $z < L_B$. The value of $A_1(\mu_i)$ at $\mu_i = 1$ is consistent with the normal-incidence reflectivity experiment. Thus, we have: $A_1(\mu_i) = A_1(\mu_i = 1) \cdot \mu_i$ and $A_1(\mu_i = 1) = 0.7$, see Fig. 2(b).

Emitted light that is scattered within a distance $L_B < z < l$ towards the exit interface, can also be redirected by Bragg diffraction by the sets of $(11\bar{1})$ planes, which are oriented at $\theta_i = 70.5^\circ$ to the (111) planes and the surface normal. The internal-reflection coefficient $R_2(\omega, \mu_i)$ for Bragg diffraction by $(11\bar{1})$ lattice planes is modelled similarly to $R_1(\omega, \mu_i)$. Taking into account that we measure emission from many randomly-oriented crystal domains in azimuthal directions, the reflectivity $R_2(\omega, \theta_i)$ is averaged over the azimuthal angles ϕ between the LK and LU lines in reciprocal space, yielding:

$$R_2(\omega, \theta_i) = \frac{3}{\pi} \int_0^{\pi/3} A_2(\theta_i, \phi) \exp \left[- \frac{(\omega - \omega_C(\theta_i, \phi))^4}{2(\Delta\omega_C(\theta_i))^4} \right] d\phi. \quad (6)$$

The magnitude $A_2(\theta_i, \phi)$ is modelled as $A_2(\theta_i, \phi) = A_2(70.5^\circ, 0^\circ) \cdot \cos(\theta_i - 70.5^\circ) \cdot \cos(\phi)$ with $A_2(70.5^\circ, 0^\circ) = 0.7$. The total internal-reflection coefficient $R(\omega, \mu_i)$ is calculated as a sum of the $R_1(\omega, \mu_i)$ and $R_2(\omega, \cos(\theta_i - 70.5^\circ))$ modified Gaussian peaks. We expect this model of the angle- and frequency-dependent internal reflectivity to capture the essential frequency dependence of the first-order photonic stop gaps in polystyrene opals.

In the case of the titania inverse opals we apply the same escape model to explain our experimental data. However, in calculating the internal-reflection coefficient $R(\omega, \mu_i)$, Bragg diffraction from other lattice planes must also be included. This difference compared to polystyrene opals appears since titania inverse opals are more strongly photonic and the measurements were performed at higher reduced frequencies ($a/\lambda = \omega a/2\pi c$). Moreover, the resulting stop gaps occur at lower detection angles θ_e in these crystals than in the polystyrene opals, as a consequence of the lower average refractive index. Therefore Bragg's law is not a sufficient approximation of the angular dependence of the stop gap and a band structure model is employed. In the model we take into account multiple gaps from (111)

and (200) lattice planes. For the inverse opals, this model was already successfully tested on diffuse transmission experiments [21].

IV. RESULTS AND DISCUSSION

A. Spontaneous emission of R6G in polystyrene opals

Reflectivity measurements at normal incidence of polystyrene opals (Fig. 2(b)) reveal that the relative width of the first-order stop gap is $\Delta\omega/\omega \approx 0.075$. For opals with a lattice parameter $a = 365$ nm this means a stop band in the range 16100 - 17300 cm^{-1} for light escaping the crystal normally to the surface. The dye R6G emits in the range of 15000 - 20000 cm^{-1} , and hence we expect to observe directional-dependent emission of the dye from the opals with $a = 365$ nm. Figure 3(a) displays the emission spectra at selected detection angles for such doped opals. It is clearly seen that the shapes of the spectra are affected by the photonic crystal. The emission is suppressed by the crystal for $\theta_e = 0^\circ$ in the spectral range from 16000 to 17500 cm^{-1} . With increasing angle θ_e the low-frequency parts of the emission recover, and the suppressed emission range shifts to higher frequencies, as expected from Bragg's law for a photonic stop gap from a single set of lattice planes. In contrast, the shape of the spectra from an opal with a lattice parameter $a = 178$ nm remains unchanged (Fig. 3(b)). The sample is not photonic for the frequency range considered: the frequencies of R6G emission lie far below the first-order stop gap in the opal with this lattice parameter.

Before studying spontaneous emission from photonic samples we have verified the applicability of the above-mentioned model of diffuse light transport on the nonphotonic, reference samples. We use Fresnel's reflection to describe the angular-dependent internal-reflection coefficient, taking an average refractive index $n_{av} = 1.44$, which is derived from the polystyrene filling fraction $\varphi \approx 74\%$ in opals and the refractive index of polystyrene $n = 1.59$. We record the intensity at the maximum of the emission spectrum as a function of the exit angle θ_e relative to the measurement at $\theta_e = 0^\circ$. The relative intensity $I(\theta_e)$ is compared to the escape function $P(\theta_e)$ in Figure 4. While the expected decrease with angle is observed, it is clear that the calculated intensity differs systematically from the measured data. This deviation appears to be caused by an angle-dependent detection efficiency as a result of an increase with θ_e of the projection of the spectrometer slit on the sample. Correcting

the measured intensity $I(\omega, \mu_e)$ for the detection efficiency $D(\mu_e)$ (see Appendix) yields the corrected intensity $I_c(\omega, \mu_e) = I(\omega, \mu_e)/D(\mu_e)$ displayed as red symbols in Fig. 4. The agreement between the corrected intensity and the calculated escape function is excellent. With the proper account of the detection efficiency, the angular distribution of emission escaping the reference samples is thus fully understood. In all experimental data presented in the remainder of this paper the detection efficiency has been included.

In the case of the photonic samples the exit distribution of emission strongly depends on the frequency ω as mentioned above: $P(\omega, \theta_e) = I_c(\omega, \theta_e)/I_{tot}(\omega)$. The total emission spectrum $I_{tot}(\omega)$ is determined by discretely summing the angle-resolved spectra $I_c(\omega, \theta_e)$ weighted by $2\pi \sin(\theta_e)d\theta_e$ to approximate the integration over 2π solid angle. The spectra from Figure 3(a) divided by the total emission spectrum $I_{tot}(\omega)$ are plotted in Figure 5 (symbols) together with the calculated escape function $P(\omega, \theta_e)$ (curves). We observe a good agreement between our experiment and theory. The escape function hardly varies with frequency in the low-frequency region $\leq 15600 \text{ cm}^{-1}$, while it still depends on the detection direction. In contrast, at higher frequencies strong variations are seen compared to the low-frequency range. At the exit angle $\theta_e = 0^\circ$, the escape function is significantly reduced in the spectral range from 16000 to 17500 cm^{-1} by the stop gap centered at $\omega = 16700 \text{ cm}^{-1}$ due to internal Bragg diffraction, which is described by the term $(1 - R(\omega, \mu_i))$ in Eq. (2). The change of the center frequency as well as the decrease in the attenuation of emission inside the stop gap with increasing exit angle θ_e are well described in our model by the frequency and angular dependent internal-reflection coefficient $R(\omega, \mu_i)$. At $\theta_e = 60^\circ$, the stop gap has moved out of the spectral range of R6G.

Figure 5 also shows a peculiar feature: the frequency ranges where the emission is inhibited along certain directions, adjoin with the ranges where emission is *increased* along the same directions. Such an increase appears at the blue side of the stop gap at $\theta_e = 0^\circ$ and 30° , and at the red side of the stop gap at $\theta_e = 45^\circ$ and 60° . This enhanced escape probability in the frequency range 16000 - 19500 cm^{-1} along directions that do not coincide with the stop gap is reflected in our model for $P(\omega, \mu_e)$ (Eq. (2)) as an increase of the angle-averaged internal-reflection coefficient $\bar{R}(\omega)$. The good agreement between experiments and theory confirms a qualitative attribution of such enhancements to diffuse escape effects [18], while it refutes earlier propositions of Bragg standing wave effects [33].

In Figure 6 we compare the experimentally determined intensity distributions (symbols)

for several fixed frequencies with the calculated ones (solid curves) as functions of the exit angle θ_e . The experimental values of $P(\theta_e)$ were obtained by dividing the emission $I_e(\theta_e)$ by the total emission spectrum I_{tot} and correcting for the angular aperture of the collecting lens Ω_L . For the frequency $\omega = 15000 \text{ cm}^{-1}$, below the stop gap, the distribution follows the Lambertian distribution and is similar to the exit distribution from the nonphotonic sample (Fig. 4). For the frequencies above the red edge of the stop gap we observe strongly non-Lambertian behaviour. For the frequency $\omega = 16500 \text{ cm}^{-1}$ emission is suppressed relative to the Lambertian distribution in the range of the exit angles from $\theta_e = 0^\circ$ to 20° . This range moves to larger exit angles for the frequency $\omega = 17400 \text{ cm}^{-1}$ in qualitative agreement with Bragg's law. For $\omega = 18350 \text{ cm}^{-1}$ the suppression observed around $\theta_e = 40^\circ$ is preceded by a considerable increase of emission in the angle range 0° to 20° . A qualitative explanation of this effect is as follows. Some escape directions are blocked by internal Bragg diffraction, and diffusion eventually distributes this back-reflected light along the remaining directions. Thus, light is more likely to exit the crystal along these allowed directions. From Figures 5 and 6 we conclude that the escape function is in excellent agreement with the measured angle-dependent spectra. To the best of our knowledge, the current work provides the first quantitative modelling of spontaneous emission spectra in 3D photonic crystals.

B. Spontaneous emission of quantum dots in titania inverse opals

Titania inverse opals possess a larger relative width of the first-order stop gap ($\Delta\omega/\omega \approx 0.16$) than the polystyrene opals owing to their inverse structure and high refractive index contrast ($m = 2.7$). The concomitant large modifications of the LDOS makes the inverse opals very attractive for control of propagation and spontaneous emission of light [9, 10]. Figure 7 shows emission spectra of CdSe quantum dots in a titania inverse opal with lattice parameter $a = 500 \text{ nm}$ for selected detection angles θ_e . No significant changes in the spectral shapes due to internal Bragg diffraction are observed, because the relative spectral width of the light sources ($\Delta\omega/\omega < 0.06$) is considerably smaller than the width of the stop gap of the photonic crystal. This shows that the escape distribution $P(\omega, \theta_e)$ does not vary significantly within the frequency range of the quantum dot spectrum. In contrast, a strong angular dependence of the emission intensity is apparent in Fig. 7. As a consequence, effects of Bragg diffraction are most convincingly observed by recording the angular dependencies

at the spectral maxima of the emission spectra.

In Figure 8(a) we present escape distributions from titania inverse opals with lattice parameters $a = 370$ and 420 nm at frequency $\omega = 16390$ cm^{-1} , and with a lattice parameter $a = 500$ nm at $\omega = 15870$ cm^{-1} . Both measured (symbols) and calculated (curves) values are shown. For the crystal with the lattice parameter $a = 370$ nm, for which the center frequency of the quantum dot spectrum lies below the stop gap, the escape function follows the Lambertian distribution. A large deviation from the Lambertian distribution is observed for the quantum dot emission from the crystals with the other two lattice parameters. In the crystals with $a = 420$ nm, the emission is strongly reduced in the range of the angles from $\theta_e = 0^\circ$ to 35° , and it is enhanced at higher exit angles. For the crystals with $a = 500$ nm, the suppression is shifted to the range of $\theta_e = 20^\circ$ to 45° , as expected for photonic gaps at higher reduced frequency ($a/\lambda = \omega a/2\pi c$), and in excellent with our theoretical predictions. The stop-band ranges are noticeably wider than that in the case of the polystyrene opals (Fig. 6), which is due to a wider frequency range of the stop gap in the titania inverse opals. To the best of our knowledge, this is the first demonstration of photonic crystal gaps in the emission spectra of confined excitons in quantum dots.

Figure 8(b) shows the photonic band structure for a titania inverse opal. The hatched regions indicate the stop band caused by Bragg diffraction by (111) lattice planes. In the angular range from $\theta_e = 35^\circ$ to 55° , multiple Bragg wave coupling from (111) and (200) diffracted waves takes place [15, 34]. The horizontal color bars represent the reduced center frequencies of the quantum dot emission from the inverse opals with the lattice parameters $a = 370, 420, 500, 580$, and 650 nm. The colors of the bars indicate the measured values of the escape function $P(\omega, \theta_e)$. For reduced frequency ranges in the range of stop gaps, it is apparent that reduced escape probability appears in the angular ranges of stop bands, whereas enhanced escape appears in ranges outside the stop bands: the light is 'squeezed' out of the crystal in the remaining allowed directions.

For experiments on quantum dot emission in photonic crystals, the good agreement between the experimentally obtained escape distributions and the calculated ones confirms that the light emanating from inside the crystals is diffuse. It also confirms that the observed emission is dominated by sources inside the bulk of the crystal. We can exclude that light sources on the sample surface contribute significantly: their emission would give rise to an angle-independent component of the intensity that is not observed. Therefore,

the spontaneous emission rates from the sources is determined by photonic LDOS effects. This observation is important for successful lifetime experiments or other quantum-optical studies of light sources in photonic crystals.

Based on the close accordance of the experiments with the model, we can extract the angle-averaged internal-reflection coefficient $\bar{R}(\omega)$. Figure 9 shows that $\bar{R}(\omega)$ is as large as 50% for the titania inverse opals and up to 20% for the polystyrene opals. The internal-reflection coefficient varies strongly with frequency in contrast to the frequency-independent \bar{R} in random media. The coefficient increases with solid angle for Bragg reflection, starting from the low-frequency edge of the L-gap. For the opals, the maximum \bar{R} occurs at the high-frequency edge of the L-gap, where the reflecting stop gaps extend over the largest solid angle [32]. For the inverse opals, the maximum \bar{R} occurs at higher reduced frequencies in the range of multiple Bragg wave coupling ($\omega a/2\pi c \sim 0.85$) [15]. The shoulder near 1.0 is attributed to the inclusion of (200) reflection condition in our model. In a more elaborate escape-model with additional diffraction conditions, we may expect additional peaks in the angle-averaged reflection coefficient at even higher frequencies. Since the inverse opals interact stronger with light than the opals, their stop gaps are wider and hence the angle averaged reflectivity is larger, in agreement with our observations.

A closer consideration of the reflectivity coefficients can serve to optimize the spontaneous emission yield of light sources (atoms, dyes or quantum dots) embedded inside thick photonic crystals ($L > l$). Such an optimization can be achieved either via the excitation of the sources, via their emission, or both. First, the excitation efficiency can be increased by realizing that increased escape probability also implies an increased probability for excitation light to enter a photonic crystal. Thus, by tuning an excitation beam to frequencies and angles of high escape, the combined action of diffusion and Bragg diffraction retain relatively more excitation light inside the sample, thus increasing the probability for spontaneous emission of the embedded light sources. Secondly, spontaneously emitted radiation is efficiently channeled out of the sample along particular directions. This occurs when the lattice parameter of the photonic crystal is chosen such that the emission frequencies are in the range of enhanced $\bar{R}(\omega)$. A clear example of enhanced escape is apparent in Fig. 5 at $\theta_e = 0^\circ$ near 18000 cm^{-1} . In the ultimate case of a photonic band gap, it has even been predicted that the diffuse emission is extremely directional, see Ref. [21]. Thirdly, one can envision situations where *both* excitation and emission are enhanced: In Fig. 8(b) enhanced

escape probability occurs both at $\omega a/2\pi c \sim 0.85$ and $\theta_e = 0^\circ$ and at $\omega a/2\pi c \sim 0.7$ and $\theta_e = 50^\circ$. Thus, by tuning the excitation to the former condition and the emission to the latter, the spontaneous emission yield is expected to be enhanced by at least a factor of two. Further improvements should be feasible in photonic crystals with even larger \bar{R} .

V. CONCLUSIONS

We have presented experimental data on angular resolved emission from light sources embedded in efficient 3D photonic crystals. The experiments were compared in detail to a recently developed model of light transport in real photonic crystals that are influenced by disorder. Our model is based on diffusion of light due to scattering (disorder) combined with angle- and frequency-dependent internal reflections (order). Good quantitative agreement between experiment and theory confirms that the details of the emission spectra are determined by the intricate interplay of order and disorder. Properties of the stop gaps, such as their frequency range, magnitude, and angular dependence, are extracted from the experiment by analyzing the emission escape function. The *enhanced* escape probability for emission along directions outside the stop gaps is explained by the angle-averaged internal-reflection coefficient $\bar{R}(\omega)$. The diffuse and angular-dependent nature of light escaping from the photonic crystals proves that the light comes from emitters *inside* the crystals. By measuring the escape functions of the quantum dot emission from the titania inverse opals, we have for the first time revealed clear stop gaps in the quantum dot emission spectra, confirming that the confined excitons experience optical confinement. The quantitative agreement between experiment and theory demonstrates that light propagation and spontaneous emission in real 3D photonic crystals is well understood.

VI. ACKNOWLEDGMENTS

We thank Floris van Driel and Daniël Vanmaekelbergh (University of Utrecht) for preparation of the quantum dots, Léon Woldering for photonic crystal preparation, Arie Irman and Karin Overgaag for experimental assistance, and last but not least Femius Koenderink for band structure calculations and discussions on escape functions. This work is part of the research program of the Stichting voor Fundamenteel Onderzoek der Materie (FOM), which

is financially supported by the Nederlandse Organisatie voor Wetenschappelijk Onderzoek (NWO).

VII. APPENDIX: MODEL OF DETECTION EFFICIENCY OF EMISSION SET-UP

The aim of this appendix is to explain the difference between the calculated escape distribution and the measured intensity illustrated in Fig. 4. This difference appears because the width of the projection of the collection optics (the spectrometer slit) on the sample increases with the angle θ_e . The sample surface is placed in the focus of the collecting lens L_1 , the spectrometer slit is in the focus of the imaging lens L_2 (*cf.* Fig. 1). The only emission collected emanates from the region confined by the slit projection on the sample surface, see Fig. 10. This means that the spectrometer collects light from a larger region on the surface at larger detection angles, and that the measured angle-dependent intensity should be corrected for the detection efficiency of the set-up. The detection efficiency is modelled as a ratio $D(\mu_e)$ of the intensity $B(\mu_e)$ collected from the surface region within the slit projection (Fig. 10) at detection angle $\theta_e = \cos^{-1}(\mu_e)$ to the intensity $B(\mu_e = 1)$ collected at normal angle:

$$D(\mu_e) = \frac{B(\mu_e)}{B(\mu_e = 1)}, \quad B(\mu_e) = \int_0^{x(\mu_e)} \int_0^{y_0} I(x, y) dx dy. \quad (7)$$

We take into account that the integration runs over a quarter of the slit, as $x(\mu_e) = x_0/\mu_e$ is the half-width of the slit projection, x_0 and y_0 are the half-width and the half-height of the slit projection at $\mu_e = \cos(\theta_e) = 1$, respectively. Typical values of x_0 and y_0 in the experiments are 50 μm and 1 mm. It is assumed that the intensity of diffuse light on the sample surface around the pump beam varies as $I(r) \propto l^2/(l^2 + r^2)$, where $r^2 = x^2 + y^2$ is the distance from the axis of the pump beam along the sample surface, and l is the mean free path of light in the sample.

-
- [1] C.M. Soukoulis, ed., *Photonic Crystals and Light Localization in the 21st Century* (Kluwer, Dordrecht, 2001).
 - [2] V.P. Bykov, Sov. J. Quant. Electron. **4**, 861 (1975).
 - [3] E. Yablonovitch, Phys. Rev. Lett. **58**, 2059 (1987).
 - [4] S. John, *ibid.* **58**, 2486 (1987).
 - [5] N. Vats, S. John, and K. Busch, Phys. Rev. A **65**, 043808 (2002).
 - [6] Y. Yang, M. Fleischhauer, and S.-Y. Zhu, Phys. Rev. A **68**, 043805 (2003).
 - [7] R. Sprik, B. A. van Tiggelen, and A. Lagendijk, Europhys. Lett. **35**, 265 (1996).
 - [8] K. Busch and S. John, Phys. Rev. E **58**, 3896 (1998).
 - [9] A.F. Koenderink, L. Bechger, H.P. Schriemer, A. Lagendijk, and W.L. Vos, Phys. Rev. Lett. **88**, 143903 (2002).
 - [10] P. Lodahl, A.F. van Driel, I.S. Nikolaev, A. Irman, K. Overgaag, D. Vanmaekelbergh, and W.L. Vos, Nature, **430** (at press, 2004).
 - [11] V.N. Bogomolov, S.V. Gaponenko, I.N. Germanenko, A.M. Kapitonov, E.P. Petrov, N.V. Gaponenko, A.V. Prokofiev, A.N. Ponyavina, N.I. Silvanovich, and S.M. Samoilovich, Phys. Rev. E **55**, 7619 (1997).
 - [12] A. Blanco, C. Lòpez, R. Mayoral, H. Miguez, F. Meseguer, A. Mifsud, and J. Herrero, Appl. Phys. Lett. **73**, 1781 (1998).
 - [13] M. Megens, J.E.G.J. Wijnhoven, A. Lagendijk, and W.L. Vos, J. Opt. Soc. Am. B **16**, 1403 (1999).
 - [14] Y.A. Vlasov and D.J. Norris, Appl. Phys. Lett. **76**, 1627 (2000).
 - [15] H.P. Schriemer, H.M. van Driel, A.F. Koenderink, and W.L. Vos, Phys. Rev. A **63**, 011801 (2001).
 - [16] Y. Lin, J. Zhang, E.H. Sargent, and E. Kumacheva, Appl. Phys. Lett. **81**, 3134 (2002).
 - [17] A.F. Koenderink and W.L. Vos, arxiv.org/abs/physics/0406052 (2004).
 - [18] L. Bechger, P. Lodahl, and W.L. Vos, submitted (2004).
 - [19] A.F. Koenderink, P.M. Johnson, J.F. Galisteo Lòpez, and W.L. Vos, C. R. Physique **3**, 67 (2002).
 - [20] J.F. Galisteo Lòpez, E. Palacios-Lidòn, E. Castillo-Martínez, and C. Lòpez, Phys. Rev. B **68**,

- 115109 (2003).
- [21] A.F. Koenderink and W.L. Vos, Phys. Rev. Lett. **91**, 213902 (2003); submitted (2004).
 - [22] J.E.G.J. Wijnhoven, L. Bechger, and W.L. Vos, Chem. Mater. **13**, 4486 (2001).
 - [23] J.R. Lakowicz, *Principles of Fluorescence Spectroscopy* (Second Edition), Kluwer, New-York, (1999).
 - [24] B.O. Dabbousi, J. Rodriguez-Viejo, F.V. Mikulec, J.R. Heine, H. Mattoussi, R. Ober, K.F. Jensen, and M.G. Bawendi, J. Phys. Chem. B **101**, 9463 (1997).
 - [25] C. de Mello Donega, S.G. Hickey, S.F. Wuister, D. Vanmaekelbergh, and A. Meijerink, J. Phys. Chem. B **107**, 489 (2003).
 - [26] A.F. Koenderink, M. Megens, G. van Soest, W.L. Vos, and A. Lagendijk, Phys. Lett. A **268**, 104 (2000).
 - [27] A. Lagendijk, R. Vreeker, and P. de Vries, Phys. Lett. **136A**, 81-88 (1989).
 - [28] J.X. Zhu, D.J. Pine, and D.A. Weitz, Phys. Rev. A **44**, 3948 (1991).
 - [29] D.J. Durian, Phys. Rev. E **50**, 857 (1994).
 - [30] The average refractive index of a photonic crystal is estimated as: $n_{av} = \varphi \cdot n_m + (1 - \varphi) \cdot n_{air}$, where φ is the volume fraction of the solid material, n_m and n_{air} are refractive indices of the solid material and air, respectively.
 - [31] F.J.P. Schuurmans, D. Vanmaekelbergh, J. van de Lagemaat, and A. Lagendijk, Science **284**, 141 (1999).
 - [32] M.S. Thijssen, R. Sprik, J.E.G.J. Wijnhoven, M. Megens, T. Narayanan, A. Lagendijk, and W.L. Vos, Phys. Rev. Lett. **83**, 2730 (1999).
 - [33] A.G. Galstyan, M.E. Raikh, and Z.V. Vardeny, Phys. Rev. B **62**, 1780 (2000).
 - [34] H.M. van Driel and W.L. Vos, Phys. Rev. B **62**, 9872 (2000).

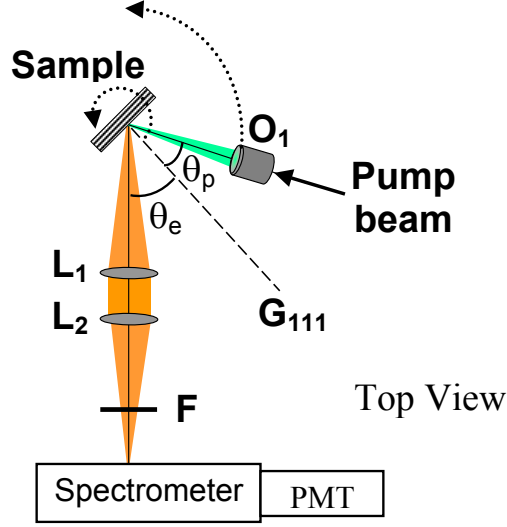


FIG. 1: (color online) Scheme of the experimental set-up. The pump beam is focused onto the sample at incident angle θ_p by the objective O_1 ($f = 7.3$ cm, $NA = 0.05$). Luminescence within a cone centered at detection angle θ_e relative to the surface normal is collected by the lens L_1 ($f = 12$ cm) and imaged on the spectrometer slit by the lens L_2 ($f = 12$ cm). A colour filter F prevents scattered pump light from entering the prism spectrometer. The angle θ_e is varied by rotating the rotation stage, which carries the sample holder, the fiber, and the objective O_1 , whereas the incident angle θ_p is kept fixed.

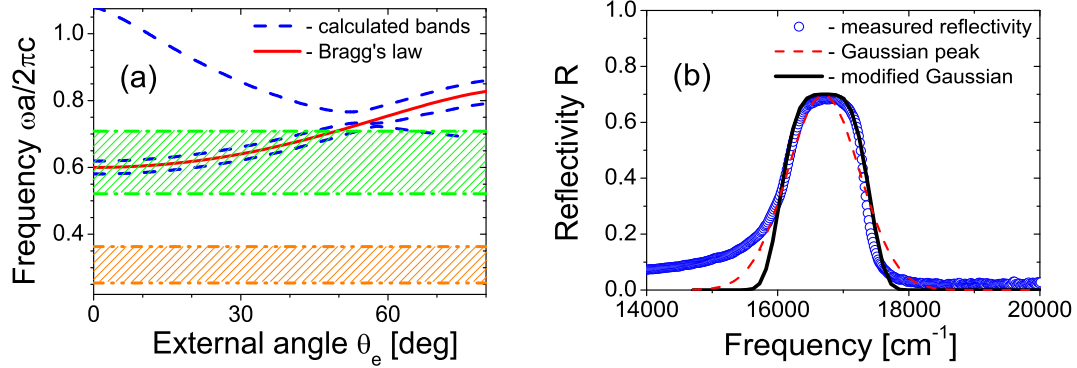


FIG. 2: (color online) (a) Photonic band structure for polystyrene opals (blue dashed curves), center frequency of the stop gap vs. detection angle θ_e according to Bragg's law (red curve), the frequency range of R6G emission is shown for opals with lattice parameters $a = 178$ and 365 nm (hatched regions between the orange dash-dot-dotted lines and the green dash-dotted lines, respectively). (b) Normal-incidence reflectivity as a function of frequency for polystyrene opals with a lattice parameter $a = 365$ nm and refractive-index contrast $m = 1.59$. Blue circles are measured values, the black curve is a fit with the modified Gaussian reflectivity peak (Eq.(6)), the red dashed curve is a fit with a Gaussian reflectivity peak.

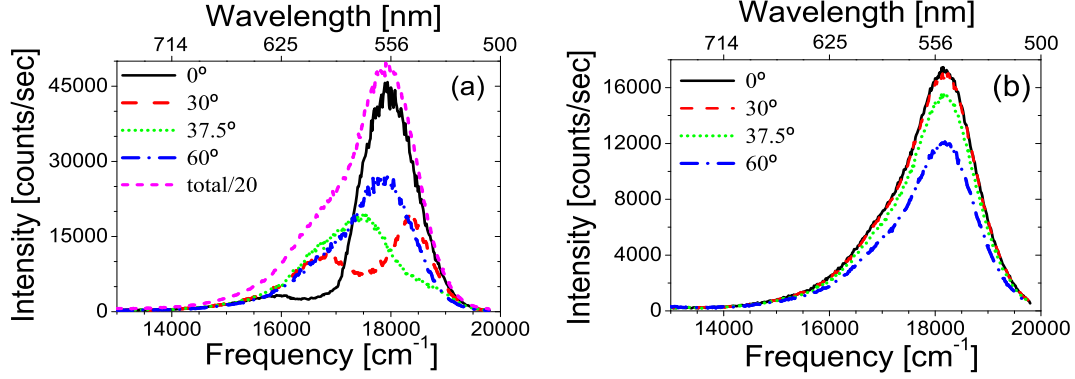


FIG. 3: (color online) Emission spectra of R6G in polystyrene opals with lattice parameters $a = 365$ nm (a) and $a = 178$ nm (b). The black curves are obtained at $\theta_e = 0^\circ$, the red dashed curves at $\theta_e = 30^\circ$, the green dotted curves at $\theta_e = 37.5^\circ$, and the blue dash-dotted curves at $\theta_e = 60^\circ$. The magenta short-dashed curve in (a) indicates the total emission spectrum $I_{tot}(\omega)$.

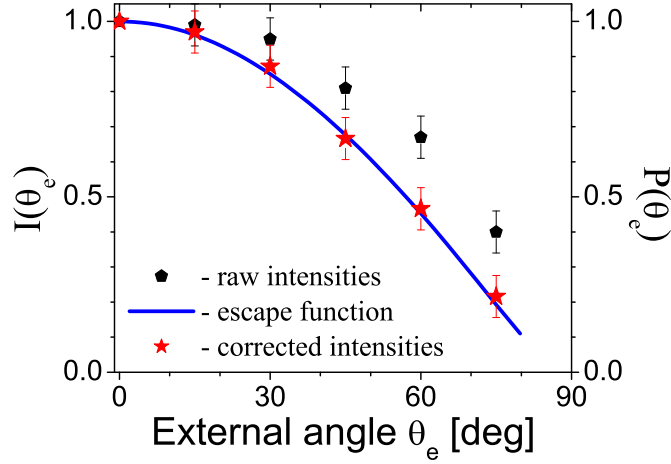


FIG. 4: (color online) Angular distribution of the R6G emission from a polystyrene opal with a lattice parameter $a = 178$ nm. The black pentagons indicate the intensity measured at the spectral maximum ($\omega = 17860$ cm⁻¹ or $\lambda = 560$ nm), the blue curve is the calculated escape function with Fresnel's internal-reflection coefficient. Measured intensities corrected for the detection efficiency of the set-up are displayed as red stars. All data are normalized at $\theta_e = 0^\circ$.

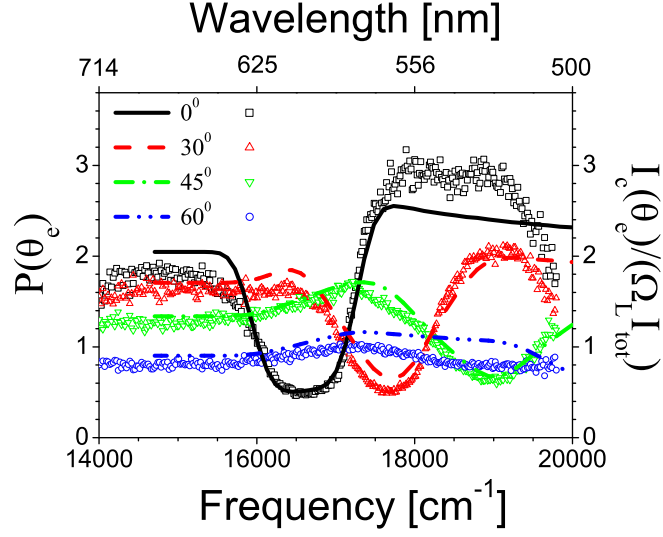


FIG. 5: (color online) R6G emission from polystyrene opal with lattice parameter $a = 365$ nm. The scatter plots represent the measured spectra corrected for the angular aperture of the collecting lens Ω_L and divided by the total emission spectrum $I_{tot}(\omega)$. The calculated escape functions are plotted with solid curves. The black solid curve and squares are for $\theta_e = 0^\circ$, red dashed curve and triangles are for $\theta_e = 30^\circ$, green inverted triangles and solid curve are for $\theta_e = 45^\circ$ and blue circles with dash-dotted curve are for $\theta_e = 60^\circ$.

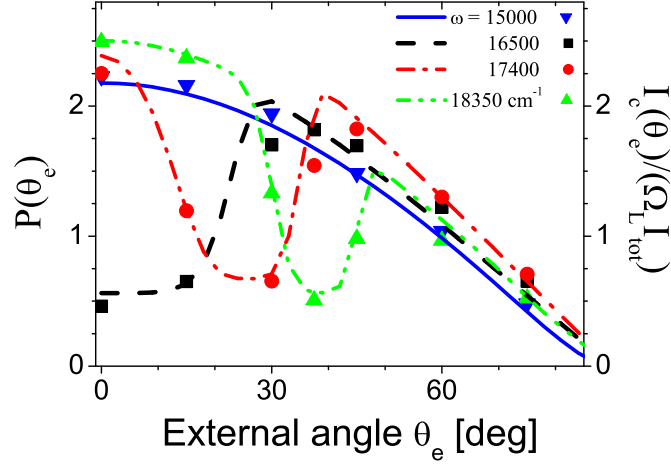


FIG. 6: (color online) Intensity ratios $I_c(\theta_e)/I_{tot}$ corrected for the lens aperture Ω_L as a function of the exit angle θ_e for a polystyrene opal with a lattice parameter $a = 365$ nm for frequencies $\omega = 15000, 16500, 17400$ and 18350 cm^{-1} (blue inverted triangles, black squares, red circles and green triangles). The corresponding curves represent the calculated escape distributions (for reduced frequencies $\omega a/2\pi c = 0.55, 0.6, 0.64$ and 0.67 , respectively).

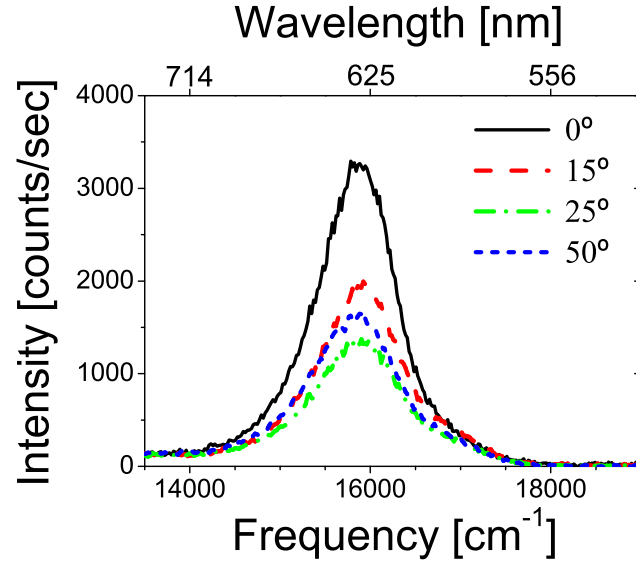


FIG. 7: (color online) Emission spectra of CdSe quantum dots in a titania inverse opal with a lattice parameter $a = 500$ nm. The black curve is obtained at $\theta_e = 0^\circ$, the red dashed curve at $\theta_e = 15^\circ$, the green dash-dotted curve at $\theta_e = 25^\circ$, and the blue short-dashed curve at $\theta_e = 50^\circ$.

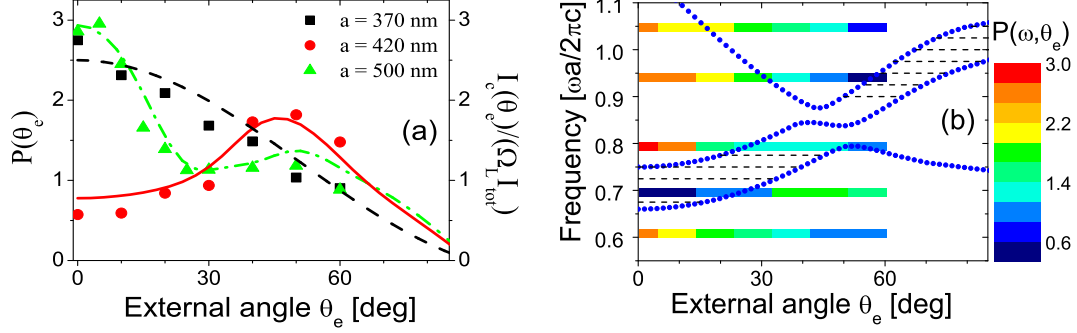


FIG. 8: (color) (a) Escape distribution as a function of the exit angle θ_e for titania inverse opals with lattice parameters $a = 370$ and 420 nm at frequency $\omega = 16390 \text{ cm}^{-1}$ ($\lambda = 610$ nm, black squares and red circles, respectively), and with a lattice parameter $a = 500$ nm at $\omega = 15870 \text{ cm}^{-1}$ ($\lambda = 630$ nm, green triangles). The corresponding curves represent the calculated distributions. (b) Photonic band structure for the inverse opals (blue dotted curves). The hatched regions indicate the stop band caused by Bragg diffraction by (111) lattice planes. The horizontal bars represent the reduced center frequencies of the quantum dot emission from the crystals with lattice parameters (bottom to top) $a = 370, 420, 500, 580$, and 650 nm. The colours of the bars indicate the measured values of the escape function $P(\omega, \theta_e)$.

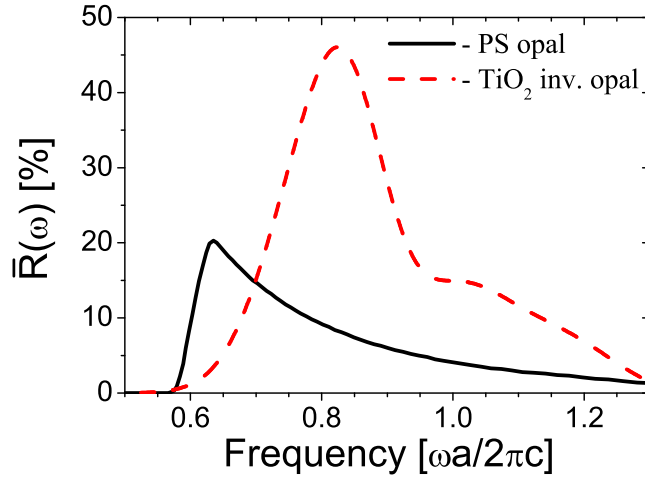


FIG. 9: (color online) The angle-averaged internal reflectivity $\bar{R}(\omega)$ for the polystyrene opals (black curve) and for the titania inverse opals (red dashed curve) according to the diffusion model, in which only the first-order Bragg diffraction is taken into account. $\bar{R}(\omega)$ determines the enhancement of the escape probability outside a stop gap direction.

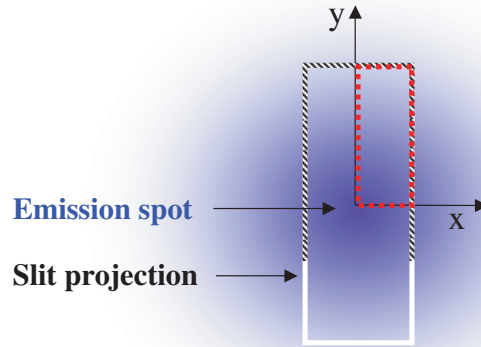


FIG. 10: (color online) Real-space cartoon of the projection of the spectrometer slit (striped rectangle) on the sample surface overlapped with the emission spot (in blue). The quarter of the slit projection (red dashed rectangle) has one of the corners in the emission-spot as center. The width of the projection (along x) increases at larger detection angles θ_e .